ORNL/TM-2016/563

Embedded Sensors and Controls to Improve Component Performance and Reliability – Loop-scale Testbed Design Report

Alexander Melin
Roger Kisner

September 2016

Approved for public release.
Distribution is unlimited.

OAK RIDGE NATIONAL LABORATORY
MANAGED BY UT-BATTELLE FOR THE US DEPARTMENT OF ENERGY

ORNL/TM-2016/563

Electrical and Electronics Systems Research Division

EMBEDDED SENSORS AND CONTROLS TO IMPROVE COMPONENT PERFORMANCE AND RELIABILITY – LOOP-SCALE TESTBED DESIGN REPORT

Alexander Melin
Roger Kisner

Date Published: September 2016

Prepared by
OAK RIDGE NATIONAL LABORATORY
P.O. Box 2008
Oak Ridge, Tennessee 37831-6285
managed by
UT-Battelle, LLC
for the
US DEPARTMENT OF ENERGY
under contract DE-AC05-00OR22725

CONTENTS

LIST OF FIGURES v
LIST OF TABLES vii
ACRONYMS ix
ABSTRACT 1
1. INTRODUCTION 1
2. DESIGN CONCEPT 3
3. IMPELLER FORCES 7
4. RADIAL BEARING 11
5. AXIAL BEARING 15
6. TOUCHDOWN BEARINGS 19
7. INSTRUMENTATION 21
8. CONCLUSIONS 25
9. REFERENCES 26

LIST OF FIGURES

1 Teikoku 204TF1 Pump Specifications. 3
2 3D Model of the Teikoku 204TF1 pump created after from disassembly and measurement. . 4
3 3D Model of the modified Teikoku 204TF1 pump testbed. 4
4 Close view of the combined thrust and axial magnetic bearing for the loop-scale testbed. . . 5
5 Axial force test data for a Teikoku canned rotor pump from the manufacturer. 9
6 Cross section of the testbed shaft. 11
7 Radial bearing nonlinear force for M19 steel when the rotor is in the center of the stator. . . 13
8 Radial bearing nonlinear for for M19 steel when the rotor is at the limit of its motion. 13
9 Exploded view of the axial magnetic bearing. 14
10 Thrust bearing annuli and geometric quantities. 15
11 Thrust bearing cross sectional geometry. 16
12 Thrust bearing force when centered. 17
13 Thrust bearing force at the limit of travel. 17
14 Exploded view of the thrust bearing. 18
15 Combined axial and thrust ball touchdown bearing. 19
16 Baumer: inductive sensor IR12.D06S-11123877 21
17 Baumer IR12: inductive sensor dimension drawing 21
18 Baumer IWFM: inductive sensor dimension drawing 23
19 Location of the axial position sensors on the magnetic thrust bearing 23

LIST OF TABLES

1 Teikoku 204TF1 Radial Force 7
2 Teikoku 204TF1 Axial Force 8
3 Radial Bearing Geometry 12
4 Baumer IR12 Position Sensor Technical Specification 22
5 Baumer IWFM Position Sensor Technical Specification 24

ACRONYMS

AMB	Active Magnetic Bearing
ASI	Advanced Sensors and Instrumentation
AWG	American Wire Gauge
BEP	Best Efficiency Point
DOE	Department of Energy
I&C	Instrumentation and Control
NEET	Nuclear Energy Enabling Technologies
ORNL	Oak Ridge National Laboratory

ABSTRACT

This report details the development of a magnetically suspended, canned-rotor testbed that will be used for future cross-cutting embedded instrumentation and control research for nuclear power applications. The design goal of the loop-scale testbed is to build a low-temperature pump that utilizes magnetic bearings, which will be incorporated into a water-loop to test control system performance and self-sensing techniques. Specifically, this testbed will be used to analyze control system performance in response to nonlinear and cross-coupling fluid effects between the shaft axes of motion, rotordynamics and gyroscopic effects, and impeller disturbances. The testbed will also be used to characterize the performance losses when using self-sensing position measurement techniques. Active magnetic bearings are a technology that can potentially reduce failure rates and maintenance costs in nuclear power plants. The magnetic bearing technology with its closely-coupled control system is particularly relevant to liquid salt reactors that operate at high temperatures (700 °C). Extreme environments limit the options for selecting sensors and actuators and potentially degrade their performance. Pumps used in the extreme environment of liquid salt reactors provide many engineering challenges that can be overcome with magnetic bearings and their associated embedded instrumentation and control. This report gives details on the mechanical and electromagnetic design of the loop-scale embedded instrumentation and control testbed. This research is funded by the Department of Energy's Nuclear Energy Enabling Technology program's Advanced Sensors and Instrumentation crosscutting research area and was performed by Oak Ridge National Laboratory.

1. INTRODUCTION

This document provides details on technical choices made in designing the embedded instrumentation and control (I&C) loop-scale testbed. This work was performed in direct support of developing advanced I&C for harsh environments under the Advanced Sensors and Instrumentation (ASI) of the Nuclear Energy Enabling Technologies (NEET) program. The goal of this Department of Energy (DOE) research initiative is the development of new cross-cutting technologies that can improve the functionality, performance, reliability, and safety of nuclear reactor components for existing and next generation reactor designs. Many new advanced reactor designs utilize different thermodynamic cycles and materials that make it challenging or impossible to import existing component designs - high temperatures and salt compatibility create real impediments long-term reliability. This research project is focused on bridging some of the technical gaps using embedded I&C. The technical application is that of cutting edge sensing, feedback control, and actuation techniques for a high-temperature, magnetic bearing pump testbed, which will have applicability to many reactor designs ranging from high-temperature gas turbines to molten salt reactors.

The current project takes advantage of previous research performed at Oak Ridge National Laboratory (ORNL) under the NEET ASI program. Phase I of the program developed a conceptual 700 °C pump with active magnetic bearings and a switched reluctance motor. Functional materials necessary for operation at 700 °C were identified. Alternative pump and magnetic bearing configurations were investigated and a conceptual design was created [2, 6]. The manufacturability of the conceptual design was studied in Kisner et al. [1]. Dynamic models of the conceptual design were developed including the fluid effects on rotor and feedback controls [4].

The current project phase has concentrated on development of a bench-top magnetic bearing testbed for embedded I&C research [5]. The bench-scale testbed was designed and fabricated. It has since been used to develop and test functional controls for the magnetic bearings.

For Phase II of the project, a low-temperature pump testbed for developing and testing embedded instrumentation and control during pump operation has been developed. This testbed will be integrated with a water loop to verify robustness of the instrumentation and controls to nonlinear and cross-coupling fluid effects between the shaft axes of motion, rotordynamics and gyroscopic effects, and impeller disturbances.

The report is organized as follows. In Section 2., the overall design concept of the testbed will be discussed. In Section 3., the impeller forces are calculated and the bearing force requirements are derived. In Section 4., the radial bearing electromagnetic design is analyzed. Section 5. covers analysis of the electromagnetic properties of the axial magnetic bearing. Section 6. discusses touchdown bearing choices. In Section 7., information on the position sensors used in the testbed are provided. And finally, Section 8. concludes and discusses future testbed experimental usage.

2. DESIGN CONCEPT

The design goal for this phase of the DOE project was to design and fabricate a working prototype of a magnetically suspended, canned-rotor pump that can be demonstrated on a water-loop at room temperature. To reduce the design time and fabrication costs, a commercial canned-rotor pump was chosen as the foundation of the testbed. The pump selected (a Teikoku 204TF1 with impeller) has specifications and flow characteristic as shown in Figure 1. The pump as originally designed utilizes graphite fluid bearings. To create the testbed, the original pump will be retrofitted with active magnetic bearings that will replace the graphite fluid bearings. This re-engineering requires extensive modification to the original pump but allows the use of the existing 3600 *RPM* induction motor, impeller, and volute thus significantly reducing design and fabrication costs. This pump model has a nominal flow rate of 532 L/min with a head of 73 m.

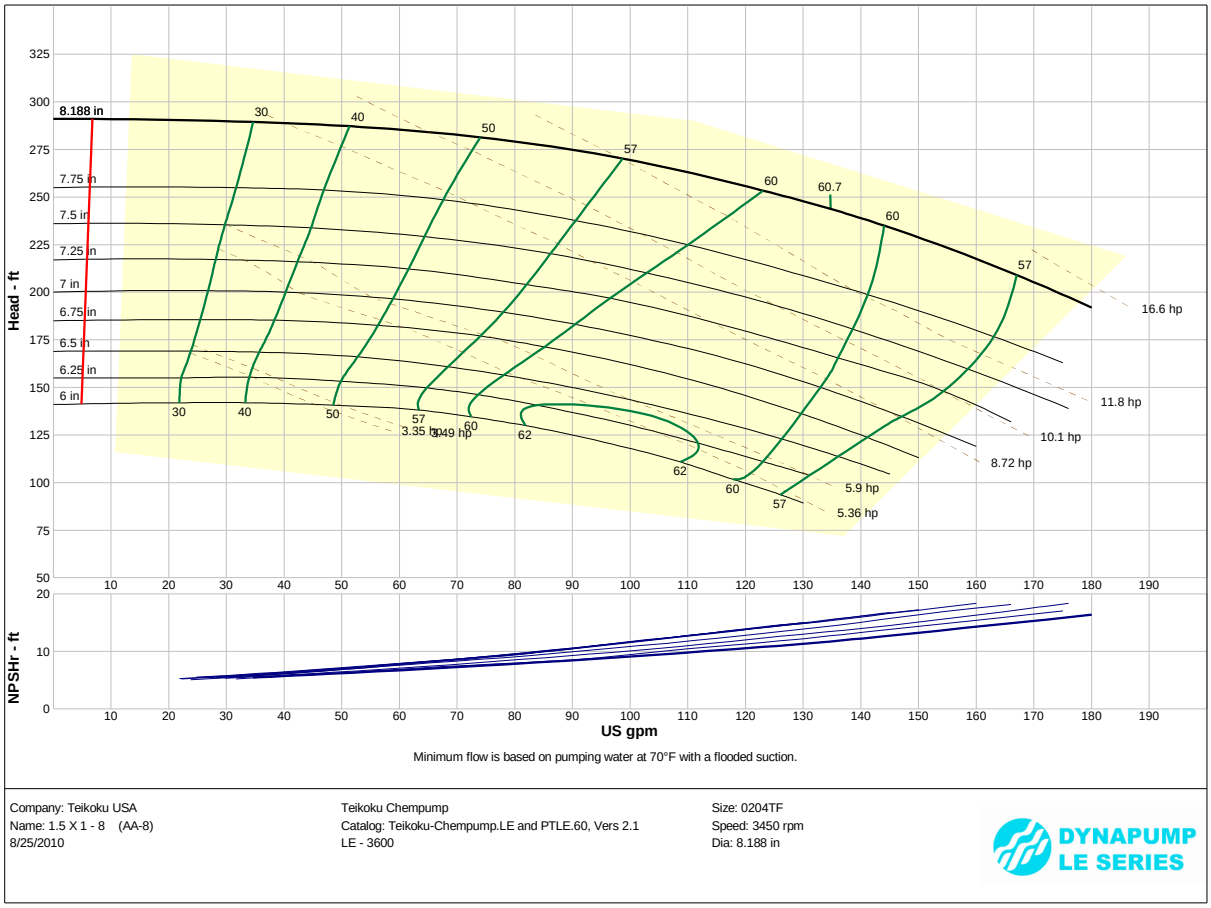

Figure 1. Teikoku 204TF1 Pump Specifications.

To accomplish the retrofit, the existing commercial pump was disassembled. Each component was then measured and modeling in 3D in SolidWorks®. The solid model rendering of the existing pump is shown in figure 2. This measurement and modeling effort was necessary because engineering drawings and solid models of the pump were unavailable from the manufacturer. Figure 3 shows the final design of the

modified Teikoku 204TF1 pump with Figure 4 showing a closer view of the thrust and axial magnetic bearing structures. The copper colored features in the illustration are the magnetic windings. The violet structures in figure 4 are the added housings to extend the original pump body to make room for the magnetic suspension. Electrical connections are made through the angled flange piece. The impeller and volute are shown at the far left in the figures.

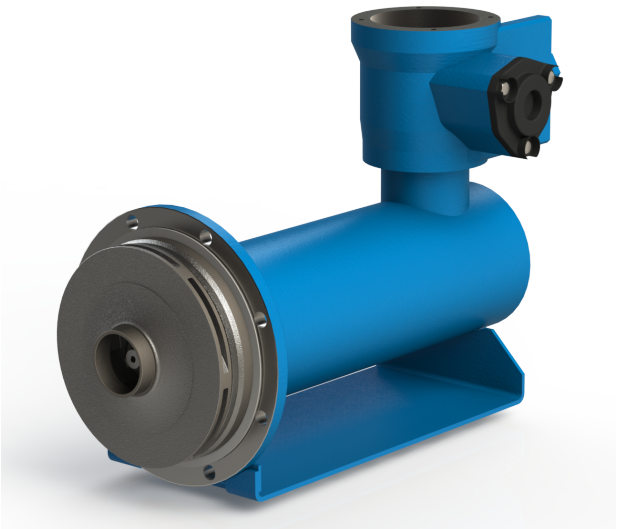

Figure 2. 3D Model of the Teikoku 204TF1 pump created after from disassembly and measurement.

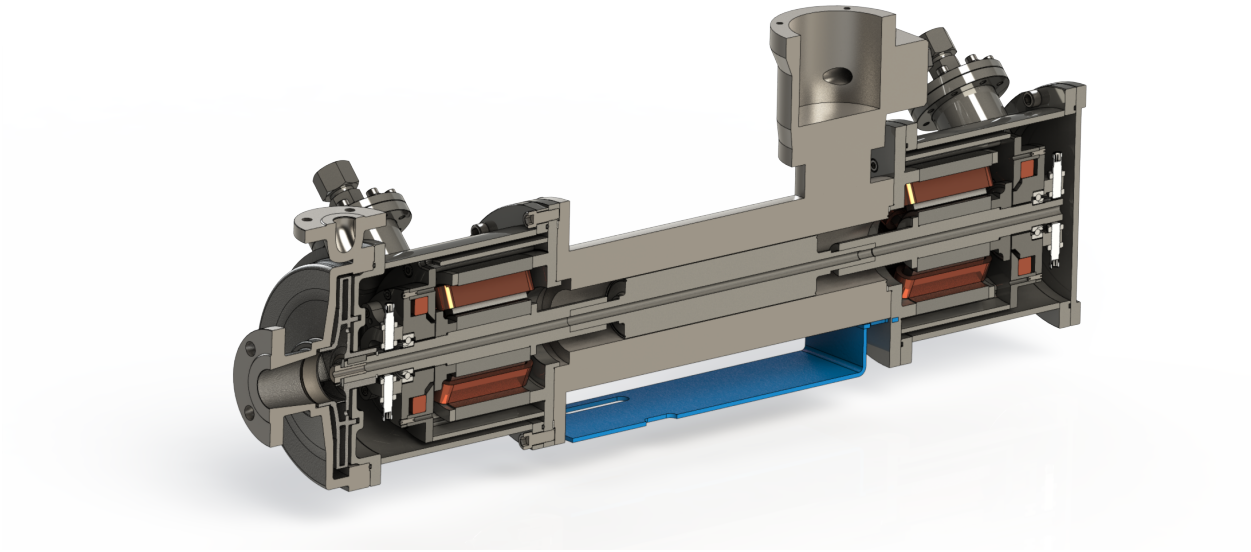

Figure 3. 3D Model of the modified Teikoku 204TF1 pump testbed.

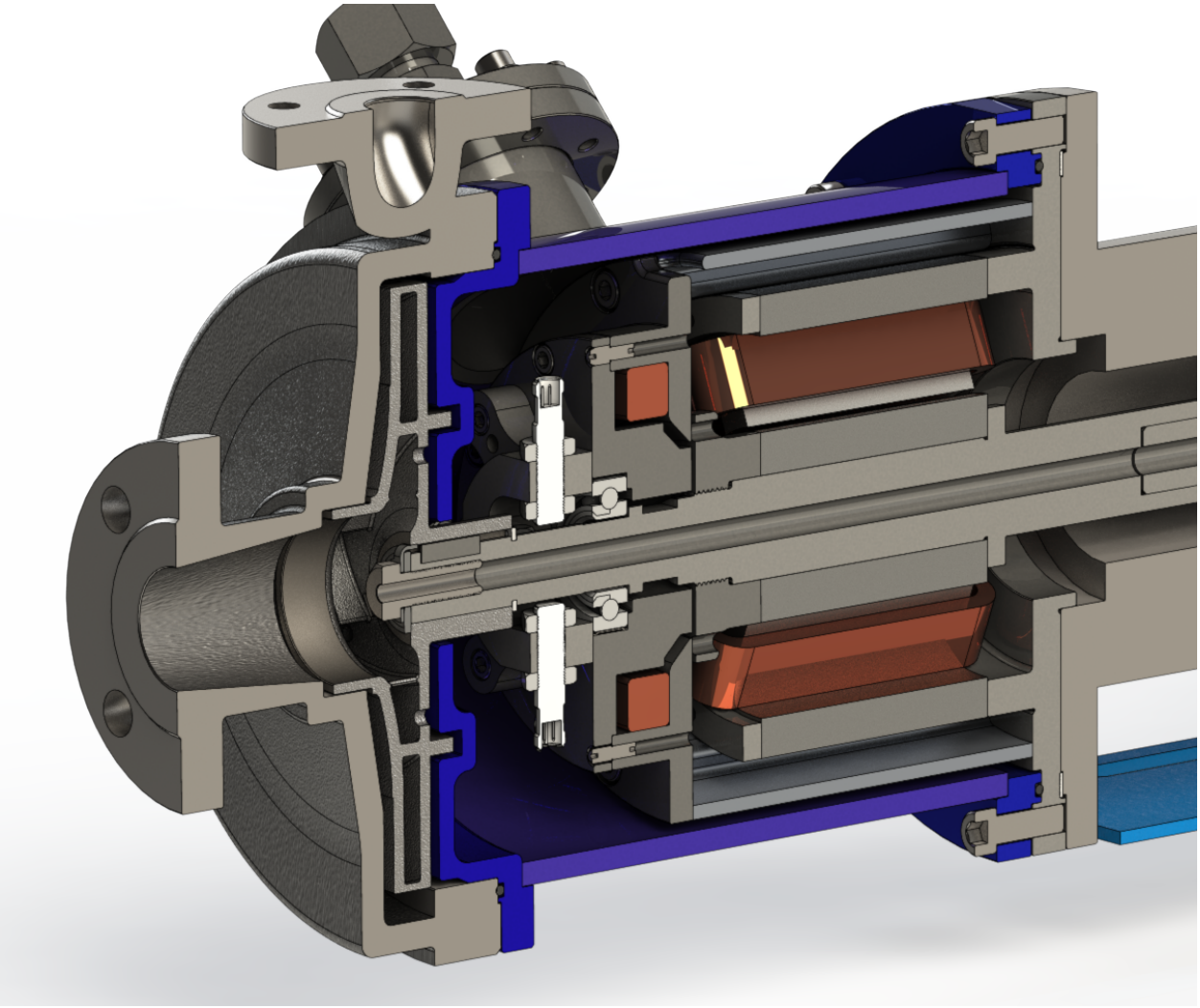

Figure 4. Close view of the combined thrust and axial magnetic bearing for the loop-scale testbed.

3. IMPELLER FORCES

The primary forces on the shaft are due to gravity and fluid forces on the impeller. To properly design the force characteristic of the magnetic bearings, the radial and axial forces created by the impeller need to be understood. The motor/pump will be mounted horizontally, so the gravitational force on the shaft will be in the radial direction.

The fluid forces on the impeller are a function of the operating conditions. The Teikoku 204TF1 pump has a single volute design, closed impellers, balance holes, and a back ring. All equations for calculating the impeller forces were taken from Lobanoff and Ross [3].

The radial loading of the pump is affected by the volute design and the fraction of operating capacity (how far from the best efficiency point (BEP)) at which the pump is operating. The radial load is given by

$$F_r = \frac{K_r H D B S_G}{102.12} \tag{1}$$

where K_r is a radial thrust factor, H is the impeller head at the flow point in m, D is the impeller diameter in mm, and B is the impeller width at the vane discharge including the shroud in mm and S_G is the specific gravity of the fluid being pumped. Table 1 summarizes the relevant physical parameters and radial forces on the Teikoku 204TF1 pump.

Table 1. Teikoku 204TF1 Radial Force

Parameter	Value	Units
K_r	(0.09, 0.38)	
H	(54.9, 88.4)	m
D	208	mm
B	16	mm
S_G	1.0	
F_r	(158.9, 1080.7)	N

The axial loading of the pump is affected by the pump flow rate and the pressure differential created between the front and rear of the impeller and the impeller design. The following force calculations are for a single-suction closed impeller with balance holes and a back ring. There are three main forces that contribute to the impeller axial forces: (1) the moment change of the fluid as it moves through the impeller, (2) the pressure differential between the front and back of the impeller, and (3) the path change moment. The moment change of the fluid due to the 90° path change from the impeller inlet to outlet causes a force F_x on the impeller that is related to the flow rate by

$$F_x = \frac{Q^2 S_G}{3.9 \times 10^6 A_I} \tag{2}$$

where Q is the flow rate in *liters per minute [lpm]*, S_G is the specific gravity of the fluid being pumped, A_I is the area of the impeller suction in m^2, and F_x is in N. The axial load on the front of the impeller F_f is given by

$$F_f = A_s P_s - (0.03 P_d (A_1 - A_s)) \tag{3}$$

Where A_s is the area of the shaft in m^2, P_s is the pump suction pressure in Pa, P_d is the pump differential pressure in Pa, A_1 is the area of the casing inlet in m^2, and F_f is the axial force on the front of the impeller in N. The axial load on the back of the impeller F_b in N is given by the equation

$$F_b = 0.75 P_d (A_1 - A_2) \tag{4}$$

where P_d is the pump differential pressure in Pa, A_1 is the area of the suction inlet in the outer casing in m^2, A_2 is the area inside the back rings on the impeller in m^2, and F_b is in N. Finally, the total axial thrust force on the impeller F_T is given by

$$F_T = F_b - F_f - F_x \tag{5}$$

where the positive ($Z+$) direction is chosen to be towards the suction inlet. The Table 2 summarizes the physical parameters and force calculations for the Teikoku 204TF1.

Table 2. Teikoku 204TF1 Axial Force

Parameter	Value	Units
Q	532	lpm
A_I	0.00248	m^2
A_s	0.00120	m^2
A_1	0.00322	m^2
A_2	0.01077	m^2
P_s	6.0×10^5	Pa
P_d	8.2×10^5	Pa
S_G	1.0	
F_x	29.2	N
F_f	22.0	N
F_b	-4645	N
F_T	-4696.2	N

These calculations indicate a large axial force on the pump which is at odds with the manufacturer's claim that the axial forces are balanced in their pump design. The maximum allowable axial force for this pump model according to the manufacturer is 600 N. This discrepancy could be partially explained by the hollow shaft design in this pump, which was not considered in Lobanoff and Ross [3]. The calculations in [3] also make assumptions about the impeller end play, wear ring gap, impeller symmetry, location of the impeller relative to the stationary walls, and balance hole geometry that are not necessarily applicable to this pump design. Because of the approximate nature of these calculations, we are using the manufacturer's maximum axial force of 600 N. This value has been verified through testing performed by the manufacturer. Test data from the manufacturer shown in Figure 5 indicates a maximum measured force of 510 N (52 kgf).

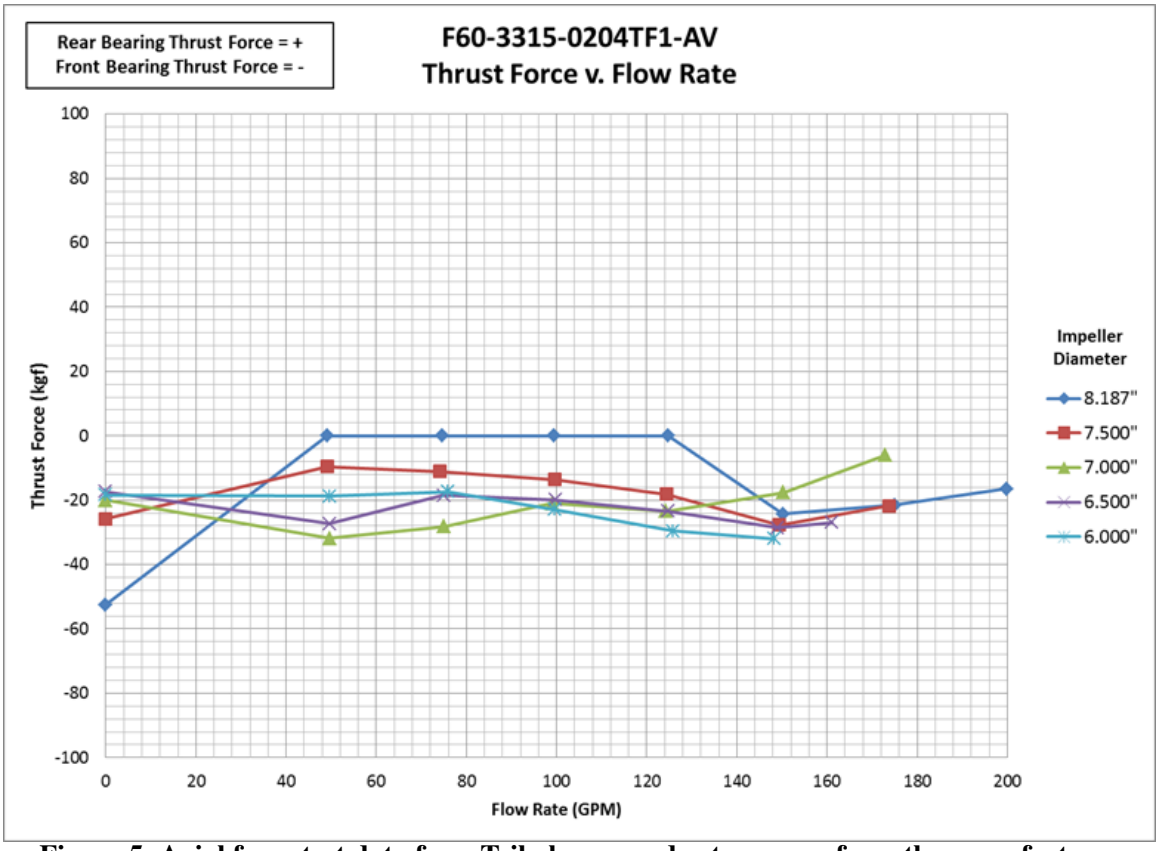

Figure 5. Axial force test data for a Teikoku canned rotor pump from the manufacturer.

4. RADIAL BEARING

The forces on both radial bearings due to fluid forces on the impeller can be calculated based on the distances from the impeller to the bearings. We will denote the impeller as the 'front' of the pump, the direction towards the impeller as $Z+$, and the radial bearing that is the closest to the impeller as the front bearing or bearing A. The bearing farthest from the impeller will be denoted as the rear bearing or bearing B. Figure 6 shows a cross-sectional view of the shaft with the relative locations and labels of the major features. The distance from bearing A to the impeller outlet denoted by L_A is approximately 0.27 m and the distance from bearing B to the impeller outlet denoted by L_B is approximately 0.860 m.

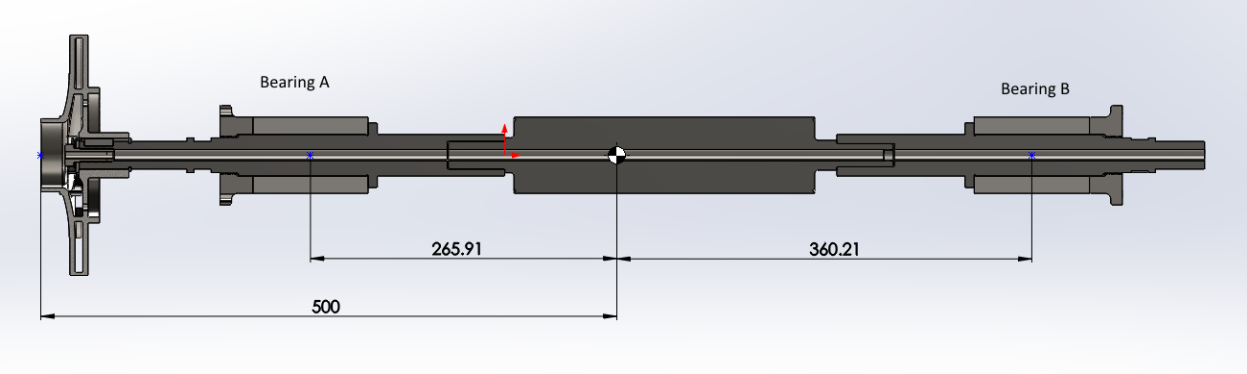

Figure 6. Cross section of the testbed shaft.

Using the following equations, the reaction forces at the bearings F_A and F_B can be calculated.

$$F_A = F_r - F_B \tag{6}$$

$$F_B = F_r \frac{L_A}{L_B} \tag{7}$$

Given a maximum radial force of $F_r = 1081\ N$, bearing A will support 742 N and bearing B will support 339 N. The bearing windings will use 16 AWG wire size, which has a nominal current limit of 20 A. For this wire size, the resistive heating at the current limit when the coil is in atmosphere will not exceed the maximum wire temperature. Although the majority of testing will occur when the coils are submerged in water, initial functional testing will occur with the coils exposed to the atmosphere so they are designed to this limiting case. Based on these current and load parameters, both front and rear radial bearings will be designed to create 2000 N force at 10 A when the shaft is centered in the stator. Table 3 gives the values for the radial bearing geometry that were derived using a custom optimization program written in Matlab® that minimizes the mass of the magnetic bearing.

The radial magnetic bearings will use a differential bearing driving mode. The force created by the radial magnetic bearing can be calculated for a rotor position x and control current u_i by

$$F = k\left(\frac{(i_0 + u_i)^2}{(x_0 - x)^2} - \frac{(i_0 - u_i)^2}{(x_0 + x)^2}\right)\cos\alpha \tag{8}$$

with

$$k = \frac{1}{4}\mu_0 N^2 A_R \tag{9}$$

Table 3. Radial Bearing Geometry

Parameter	Value	Units	Description
x_0	0.0015	m	Air Gap
i_0	8.0	A	Bias Current
d_r	0.066	m	Rotor OD
h_t	0.030	m	Tooth Height
w_t	0.0129	m	Tooth Width
h_s	0.100	m	Stack Height
N	160	$turns$	Total Coil Turns
α	22.5°	deg	Tooth Angle

Figure 7 shows both the theoretical linearized force characteristics of the radial bearing differential drive design along with the nonlinear force calculated using the material properties of M19 electrical steel which is used for the rotor and stator lamination for the radial bearings. From [7], linearizing (8) about the operating points $x = 0$ and $u_i = 0$ yields the expression of the bearing force given by

$$F_l = k_i i + k_x x \tag{10}$$

where

$$k_i = \frac{4ki_0}{x_0^2} \tag{11}$$

$$k_x = \frac{4ki_0^2}{x_0^3} \tag{12}$$

For this radial bearing design, $k_i = 136.3$ and $k_x = 727044.6$.

We also need to ensure that the bearing will have sufficient force at the limits of the radial motion to overcome weight of the shaft. The shaft has a mass of 18.3391 kg and a weight of 180 N. Figure 8 shows the nonlinear force produced by the radial bearing when it is resting on the touchdown bearings and demonstrates that the radial bearing will have sufficient force magnitudes at the limits of shaft travel to overcome the gravitational forces on the shaft.

Figure 9 shows an exploded view of the radial bearing design.

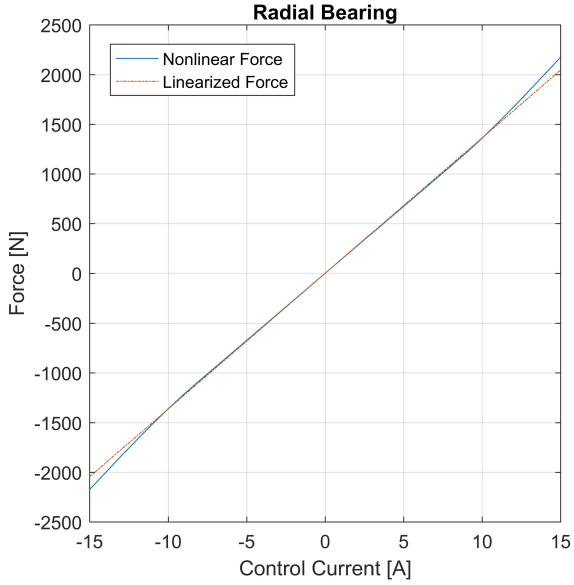

Figure 7. Radial bearing nonlinear force for M19 steel when the rotor is in the center of the stator.

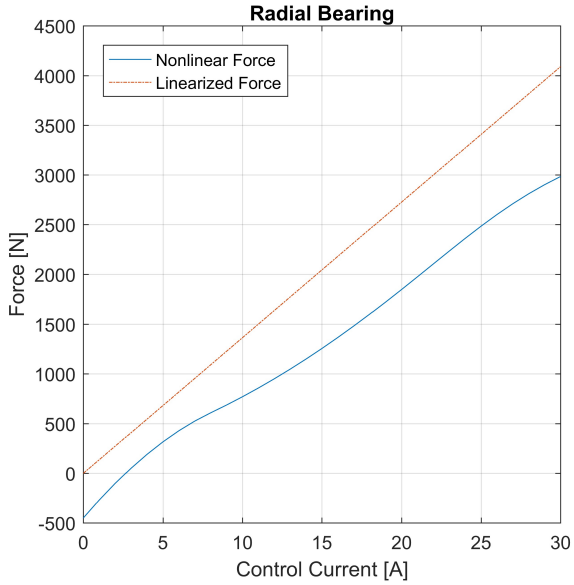

Figure 8. Radial bearing nonlinear for for M19 steel when the rotor is at the limit of its motion.

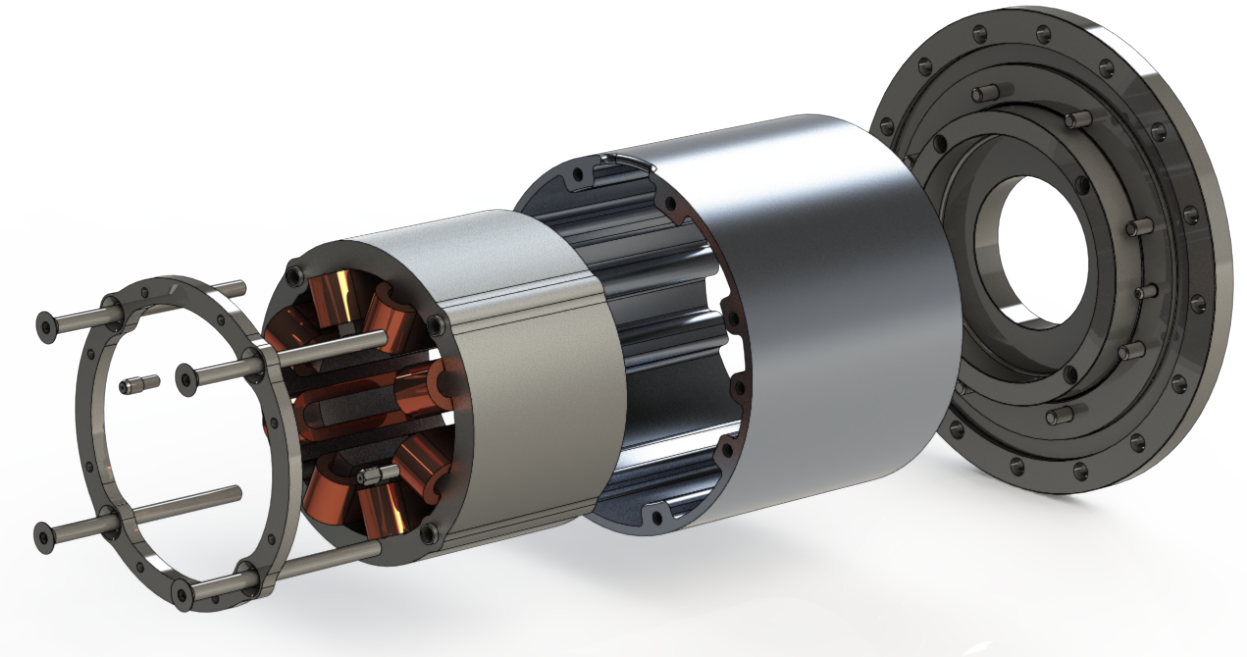

Figure 9. Exploded view of the axial magnetic bearing.

5. AXIAL BEARING

The axial bearing design will have two concentric annulus surfaces on the stator for the flux to pass through to the rotor. To maximize the magnetic flux, the area of both of these annuli should be equal. In addition, we would like to separate the outer diameter of the smaller annulus and the inner diameter of the larger annulus by a gap larger than the thrust bearing airgap to reduce the magnetic forces between them and prevent a short circuit of the magnetic flux. Given the outer radius of the larger annulus r_o, the inner radius of the smaller annulus r_i, and the gap g_a we can calculate the smaller annulus outer radius r_i^m and the larger annulus inner radius $r_o^m = r_i^m + g_a$.

$$r_i^m = \frac{1}{2}\left(-1 + \sqrt{2r_i^2 + 2r_0^2 - 2g_a + 1}\right) \tag{13}$$

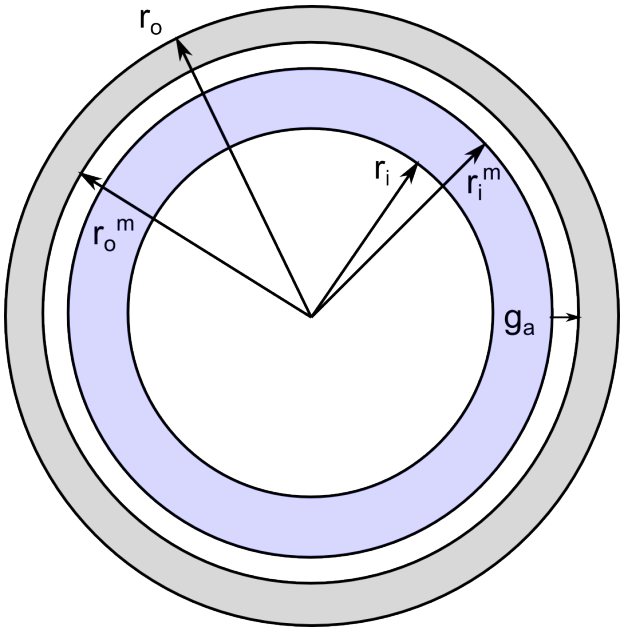

Figure 10. Thrust bearing annuli and geometric quantities.

For the Teikoku pump, we will choose a $r_o = 43\ mm$, $r_o^m = 34.2\ mm$, $r_i^m = 32.2\ mm$, and $r_i = 17\ mm$ for a 2 mm gap. Figure 11 shows a typical cross-section of the thrust bearing design. This diameter value gives a cross-sectional area of 2350 mm^2. Assuming a maximum flux density B_{max} of 1.4 T, the maximum force that can be created by the impeller side axial magnetic bearing is

$$F_{max} = \frac{B_{max}^2 A_T}{\mu_0} = 3328\ N \tag{14}$$

and the number of windings N_T to achieve the maximum magnetic flux is

$$N_T = \frac{2B_{max}z_0}{\mu_0 u_i} = 334\ turns \tag{15}$$

where $z_0 = 1.5\ mm$ is the nominal airgap and $u_i = 10\ A$ is the nominal coil current. With 16 AWG wire with a cross sectional area of 1.3 mm^2 and a packing factor of 0.6, the required winding area is 868 mm^2.

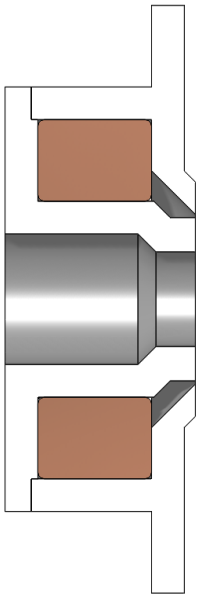

Figure 11. Thrust bearing cross sectional geometry.

With a bias current of 3.5 A and an airgap of 1.5 mm, the thrust bearing has the linearized coefficients

$$k_i = 465.4$$
$$k_x = 1085963$$

Figure 12 shows the nonlinear force when using M19 steel and the linearized force for the thrust bearing using a differential drive design (see equation 8). The maximum nonlinear force corresponds to the theoretical maximum force calculated in (14). Figure 13 shows the force response of the thrust bearing at the limit of the shaft travel. This figure shows that even at the limit of travel, the thrust bearing creates enough force to overcome the maximum expected axial force of 600 N.

Figure 14 shows an exploded view of the final thrust bearing design.

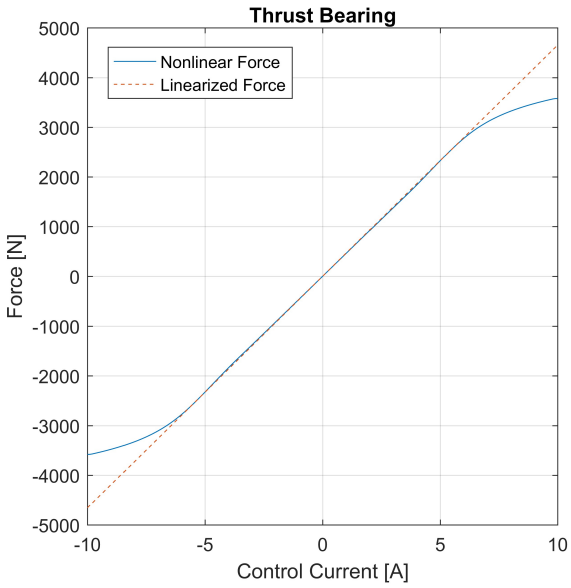

Figure 12. Thrust bearing force when centered.

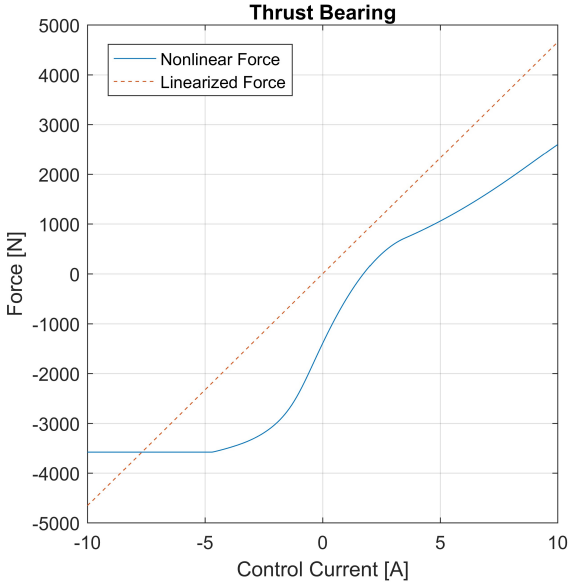

Figure 13. Thrust bearing force at the limit of travel.

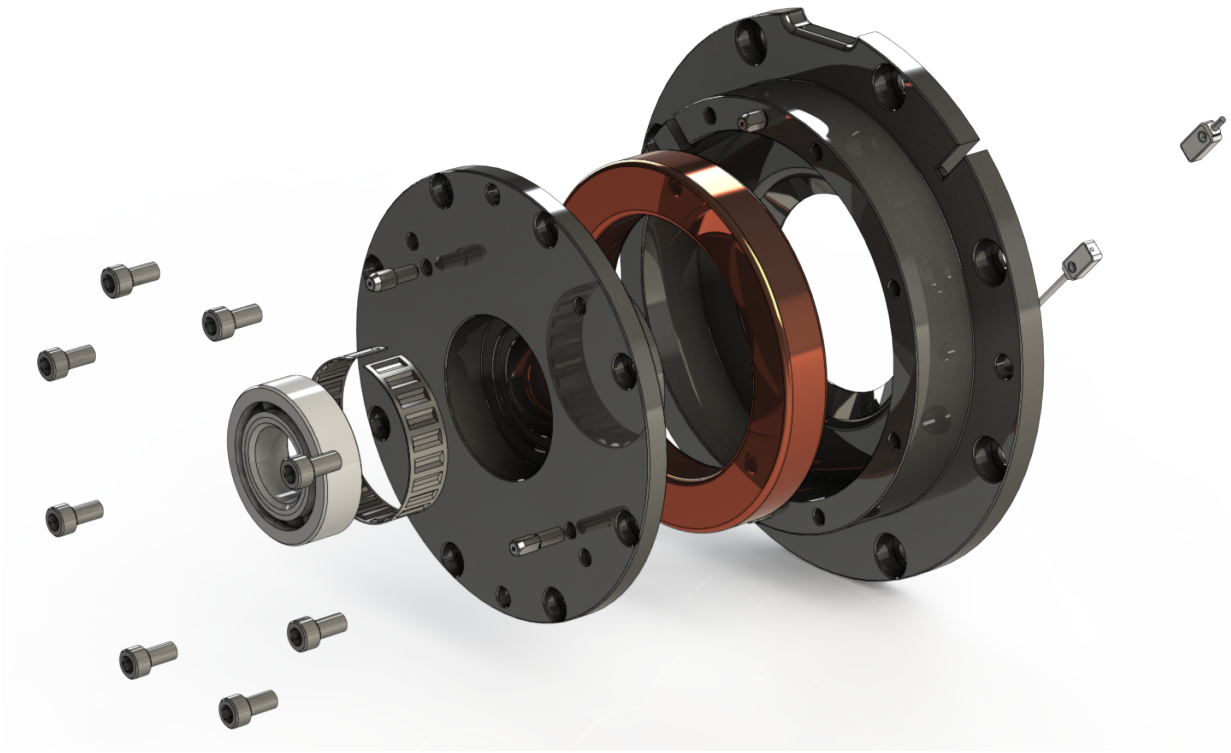

Figure 14. Exploded view of the thrust bearing.

6. TOUCHDOWN BEARINGS

Mechanical touchdown bearings are a critical component of any magnetic bearing design. They protect the rotor and stator from accidental contact during off-normal operation, provide a resting position for the rotor when the magnetic bearing is not turned on, and allow the pump to continue operation at reduced performance in the event that the magnetic bearing fails. Because this testbed will be operated at low temperatures, off-the-shelf combined thrust and axial bearings, shown in figure 15, will be used. Bearing

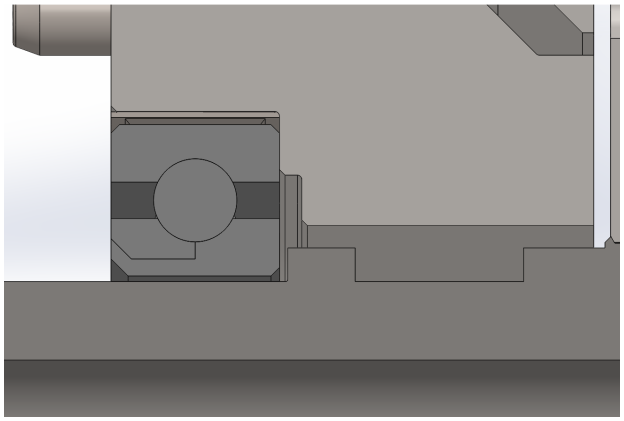

Figure 15. Combined axial and thrust ball touchdown bearing.

tolerance rings are used to mount the touchdown bearings to simplify fabrication and assembly while providing damping to the shaft in the event of rotor contact with the touchdown bearings. The radial clearance between the rotor and the touchdown bearing is 0.4 *mm* and the axial clearance is 0.75 *mm*.

7. INSTRUMENTATION

For a high-temperature application of a canned-rotor pump, using separate position sensors is almost impossible. The ultimate design goal of this magnetic suspension system is to measure position through the actuation coils. Self-sensing through the magnet coils is possible to achieve with correct modeling and design. However, for this loop-scale water pump system, accurate shaft position measurements are needed for experimental data validation during self-sensing operation. The shaft will be measured using physical sensor in a differential mode to remove any sensor bias from the measurement. Orthogonal radial measurements and an axial measurement will be taken at each end of the shaft.

For measuring the shaft position, inductive sensors were chosen over capacitive, laser metrology, and other non-contact sensor techniques. Inductive sensors offered sufficient resolution, accuracy, repeatability, noise rejection, and insensitivity to the target material in a convenient form factor and reasonable price. The radial measurement sensors selected for the testbed are Baumer IR12.D06S-11123877 shown in Figures 16 and 17. Table 4 gives the sensor characteristics.

Figure 16. Baumer: inductive sensor IR12.D06S-11123877

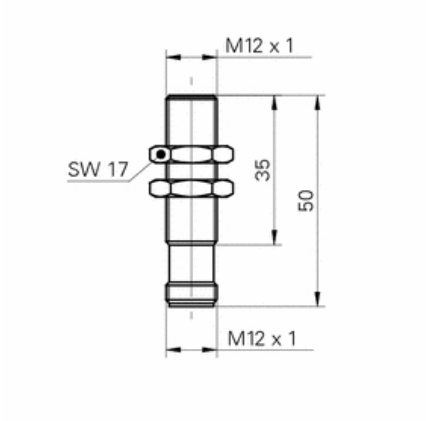

Figure 17. Baumer IR12: inductive sensor dimension drawing

The form factor of the Baumer IR12.D06S sensor makes using it for the axial measurement difficult, so a

Table 4. Baumer IR12 Position Sensor Technical Specification

General Data	
Mounting type	quasi-flush
Measuring distance Sd	$0 \ldots 6\ mm$
Resolution	$< 0,005 mm$ (stat.)
	$< 0,01 mm$ (dynam.)
Repeat accuracy	$< 0,01 mm$
Linearity error	$\pm 720 \mu m$ (S=$0 \ldots 6\ mm$)
	$\pm 300 \mu m$ (S=$1.5 \ldots 4.5\ mm$)
Temperature drift	± 6 (Full Scale; $-25 \ldots + 75\ ^\circ C$)
	± 4 (Full Scale; $0 \ldots + 60\ ^\circ C$)
Electrical Data	
Response time	$< 1\ ms$
Voltage supply range $+Vs$	$12 \ldots 36\ VDC$
Current consumption max. (no load)	$10 mA$
Output circuit	voltage output
Output signal	$0 \ldots 10\ VDC$
Load resistance	$> 4000\ Ohm$
Short circuit protection	yes
Reverse polarity protection	yes
Mechanical Data	
Type	cylindrical threaded
Housing material	brass nickel plated
Dimension	$12 mm$
Housing length	$50 mm$
Connection types	connector $M12$
Ambient Conditions	
Operating temperature	$-25 \ldots + 75\ ^\circ C$
Protection class	IP67

Baumer IWFM 08U9501 sensor was chosen. Figure 18 shows the sensor dimensions.

The Baumer IWFM sensor technical specifications are given in Table 5.

Figure 19 shows the location of the axial sensors. At this location their target is the thrust bearing rotor.

Both the Baumer IR12 and Baumer IWFM sensors have an IP67 rating. This rating will not withstand extended operation in liquid. Additional waterproofing will be required for reliable sensor operation. Consultation with Baumer engineering has led us to determine that an epoxy seal on the sensor will be sufficient for the low pressure, low temperature water environment. Signals from the sensors are processed through isolation amplifiers and sent to analog-to-digital converters for use by the control system.

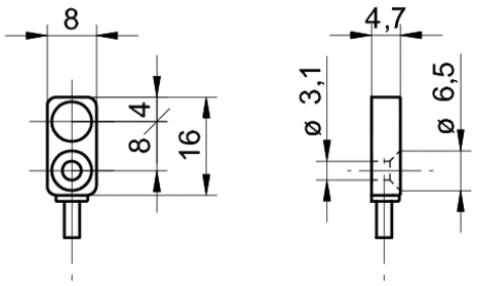

Figure 18. Baumer IWFM: inductive sensor dimension drawing

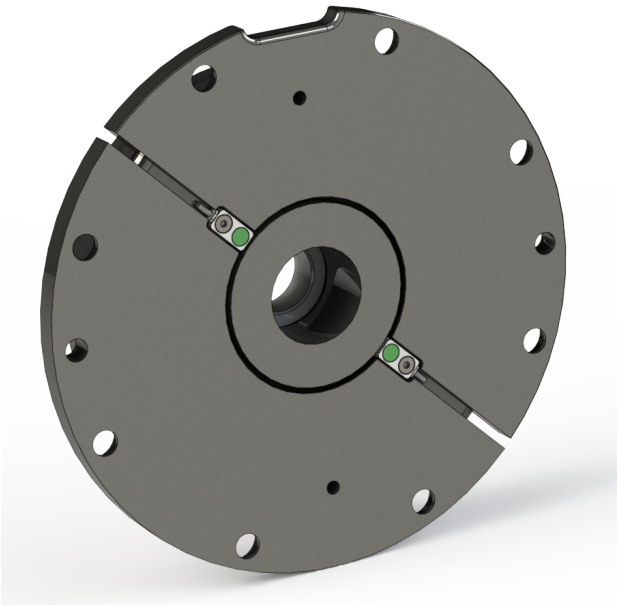

Figure 19. Location of the axial position sensors on the magnetic thrust bearing

Table 5. Baumer IWFM Position Sensor Technical Specification

General Data	
Mounting type	quasi-flush
Measuring distance Sd	$0 \cdots 2\ mm$
Resolution	$< 0,001mm$ (stat.)
	$< 0,005mm$ (dynam.)
Repeat accuracy	$< 0,02mm$
Linearity error	$\pm 100\mu m$
Temperature drift	$\pm 5\%$
Electrical Data	
Response time	$< 1\ ms$
Voltage supply range $+Vs$	$15 \ldots 30\ VDC$
Current consumption max. (no load)	$10mA$
Output circuit	voltage output
Output signal	$0 \ldots 10\ VDC$
Load resistance	$> 3000\ Ohm$
Short circuit protection	yes
Reverse polarity protection	yes
Mechanical Data	
Type	cylindrical threaded
Housing material	brass nickel plated
Dimension	$8mm$
Housing length	$16mm$
Connection types	cable
Ambient Conditions	
Operating temperature	$10 \cdots +60\ ^\circ C$
Protection class	IP67

8. CONCLUSIONS

This report details the mechanical and electromagnetic design calculations of an embedded I&C testbed that incorporates active magnetic bearings into a canned-rotor pump. This system will be fabricated and installed to test the performance of embedded instrumentation and controls under real-world conditions in FY2017. These environmental conditions include nonlinear and cross-coupling fluid effects between the shaft axes of motion, rotordynamics and gyroscopic effects, and impeller disturbances. The performance of different control design techniques will be evaluated in FY2017 along with the performance reductions associated with self-sensing bearing techniques.

This design can be extrapolated for motors operating at high temperatures in liquid salt by changing some of the materials and implementing the self-sensing position and speed measurements. Such a development would be a natural next phase of work.

9. REFERENCES

[1] Roger A. Kisner, David L. Fugate, Alexander M. Melin, David E. Holcomb, Dane F. Wilson, Pamela C. Silva, and Carola C. Molina. Evaluation of manufacturability of embedded sensors and controls with canned rotor pump system. Technical report, Oak Ridge National Laboratory ORNL/TM-2013/269, 2013.

[2] Roger A. Kisner, Alexander M. Melin, Timothy A. Burress, David L. Fugate, David E. Holcomb, John B. Wilgen, John M. Miller, Dane F. Wilson, Pamela C. Silva, Lynsie J. Whitlow, and Fred J. Peretz. Embedded sensors and controls to improve component performance and reliability: Conceptual design report. Technical report, Oak Ridge National Laboratory ORNL/TM-2012/433, 2012.

[3] Val S. Lobanoff and Robert R. Ross. *Centrifugal Pumps Design & Application*. Gulf Publishing Company, 1985.

[4] Alexander M. Melin, Roger Kisner, and David L. Fugate. Embedded sensors and controls to improve component performance and reliability: System dynamics modeling and control system design. Technical Report ORNL/TM-2013/415, Oak Ridge National Laboratory, 2013.

[5] Alexander M. Melin, Roger A. Kisner, Anis Drira, and Frederick K. Reed. Embedded sensors and controls to improve component performance and reliability - bench-scale testbed design report. Technical report, Oak Ridge National Laboratory ORNL/TM-2015/584, 2015.

[6] Alexander M. Melin, Roger A. Kisner, and David L. Fugate. Advanced instrumentation and controls for extreme environments. *IEEE Instrumentation and Measurement Magazine*, 16(3), June 2013.

[7] Alfons Traxler and Eric Maslen. *Magnetic Bearings: Theory, Design, and Application to Rotating Machinery*. Springer, 2010.